Unconventional Resources 6 (2025) 100133

Contents lists available at ScienceDirect

Unconventional Resources

journal homepage: www.keaipublishing.com/en/journals/unconventional-resources/

Mechanistic controls on permeability evolution in thermally-upgraded low-maturity oil shales: Application of machine learning outputs

Bo He [a], Lingzhi Xie [a], Xin Liu [b,c], Jun Liu [a,*], Derek Elsworth [d]

[a] Key Laboratory of Deep Underground Science and Engineering (Ministry of Education), Institute of New Energy and Low-Carbon Technology, Sichuan University, Chengdu, 610065, China
[b] State Key Laboratory of Continental Shale Oil, Daqing, 163712, China
[c] Daqing Oilfield Exploration and Development Research Institute, Daqing, 163712, China
[d] Department of Energy and Mineral Engineering, Pennsylvania State University, University Park, PA 16802, USA

ARTICLE INFO

Keywords:
S: oil shale
Seepage capacity
Qingshankou formation
Thermal upgrading
SEM scanning

ABSTRACT

In-situ thermal upgrading aids recovery from low-maturity oil shales where low permeability is the rate-limiting feature. We use machine leaning classified pore and pore network morphological descriptions recovered at elevated temperatures to define the dynamic thermal evolution of permeability. These descriptions define key factors influencing permeability evolution, in particular the development of anisotropy and its implication for recovery. Heating enhances permeability by increasing both the number and total cross-sectional area (SEM) of pores. Fractal dimensions indicate that the pore microstructure is anisotropic in the bedding-parallel and bedding-perpendicular directions and is upgraded by elevated temperature. The permeability anisotropy endures throughout the entire heating process and fluctuates at elevated temperature, quantified by the index called anisotropic coefficient of permeability. A newly proposed “aggregation degree” indexes the relative contribution of minority pores to overall permeability – 50 % of the permeability (*K*) is sourced from <8 % pores in the SEM section. Increased temperature elicits increased permeability – thus, the temperature applied at the injection well defines the flow limiting permeability threshold at the production wells and thus controls flow rates from the entire heated reservoir. This work provides fresh insights in defining the thermal permeability response of low-maturity oil shales and guides fluids recovery.

1. Introduction

The growing global demand for oil supply drives the energy revolution, prompting the need for recovery from low permeability and low-maturity reserves [1–4]. Domestic shale oil significantly supports US energy independence and has enabled the US to become a net oil exporter in 2019. This further drives technical innovation in the exploration and production of shale oil - in nature, an unconventional reserve [5,6]. Nevertheless, the shale oil development differs in different regions or/and different strata [7,8]. For some with ideal geological conditions (e.g., high-maturity shale oil), the drilling of horizontal wells and hydraulic fracturing ensures feasible extraction [9]. In comparison, low-maturity shale oil is usually not directly extractable and thus needs additional stimulus to become recoverable. Thus, in-situ thermal upgrading by artificial heating to ~300–500 °C is seen as a promising approach [10–12].

The essence of thermal upgrading is to pyrolyze the organic matter in low-maturity oil shales to then release oil/gas, during which the pore structure is changed and seepage channels developed [13,14]. This phenomenon has been observed by CT scanning – indicating that thermal cracks are induced during the heating operations – with more cracks developed at elevated temperatures [15]. The channels supporting flow change dynamically during the in-situ heating processing – with these being influential in restoring liquid transport and thus are a primary object of such characterization defining the mechanics of thermal upgrading [16,17]. Moreover, the heating-induced evolution of flow channels also determines the carbon storage potential in oil shale reservoirs [18].

Conventional wisdom suggests that heating increases the availability of reservoir flow channels. Thus, permeability evolves through this modification of the pore system as the state of organic matter-related pores evolve with a greater proportion relative to the whole pores [19,

* Corresponding author.
E-mail address: j.liu@scu.edu.cn (J. Liu).

https://doi.org/10.1016/j.uncres.2024.100133
Received 25 August 2024; Received in revised form 28 November 2024; Accepted 22 December 2024
Available online 24 December 2024

20]. Heating-induced alteration of the pore space is believed to augment flow capacity, supported by both experimental and numerical observations [21–23]. Nevertheless, this augmentation by heating is suggested to evolve through a variety of mechanisms. For example, permeability may evolve continuous continuously from 25 °C to 550 °C [24], or with a sharp decline at 350 °C–375 °C [25]. Permeability alteration may be identified as three stages, i.e., gradual increase (20 °C–30 °C) – slight decrease (300 °C–400 °C) – then sharp increase (>400 °C) [26]; in comparison, it has also been described as occurring in five stages –that is, slightly improved (25 °C–300 °C) –stable (300 °C–350 °C) – sharply declining (350 °C–375 °C) – stably increasing (375 °C–450 °C) – significantly increasing (>450 °C) [25]. These conflicting observations identify the need to link permeability evolution to tangible controlling petrophysical properties – an approach used in this following – inclusive of the important role of permeability anisotropy, and its evolution with temperature and time.

Accordingly, this work builds on previous characterizations [27] that quantitatively measured the dynamic evolution of pore morphology in low-maturity oil shales during gradual heating. This work used captured SEM images of pore structure categorized by machine learning. We now use these machine learning outputs to define mechanistic models of permeability evolution with temperature. Specifically, a Hagen-Poiseuille model connects evolving pore morphologies with Darcy's law including accommodation for evolving anisotropic permeability related to bedding-parallel and bedding-perpendicular directions. This yields predictive models to define permeability evolution based on key shale characteristics and arbitrary heating paths with application to thermal upgrading.

2. Geological background

This work uses oil shale from the Upper Cretaceous Qingshankou (UCQ, in short) formation in the Songliao basin, NE China as a typical example. The Songliao basin, a Mesozoic-Cenozoic continental sedimentary basin [28,29], occupies an area of ~260000 km^2 and is ~750 km long and 330–370 km wide [30]. During deposition, tectonic activity in multiple stages delineated six structural units, defined as the northern plunge, western slope, northeastern uplift, central depression, southwestern uplift and the southeastern uplift (Fig. 1a). The current distribution of the UCQ formation is mainly in the central depression zone and its periphery (Fig. 1a).

With respect to basin evolution, four stages are recognized, *viz.* pre-rift doming, syn-rift subsidence, post-rift thermal subsidence and structural inversion [31,32]. This basin evolution is accompanied by a series of strata representing multiple-stages at multiple-times resulting in multiple-cycles [33], during which the Cretaceous formation was formed at ~135-65 Ma [34]. During the Cretaceous period, the paleolake-level change ensured multiple occurrences of unconformities and complicated lithological association sequences, including coals, mudstones, sandstones, conglomerates and oil shales (Fig. 1b). Among these sequences, two oil shale strata from the Qingshankou and Nengjiang formations are highly charged with oil [33,35]. Although the Cretaceous strata were deposited in the freshwater Songliao paleolake, convincing evidence indicates that saline conditions existed during sedimentation, due to the influx of seawater during marine transgression [36].

3. Experimental and analytical methods

Following collection, the UCQ oil shale samples were prepared for SEM quantitative imaging. We follow the methodology for obtaining parameters of pore morphology at in-situ elevated temperature as detailed by Liu et al. [27]. This is the basis for the permeability investigations of this work.

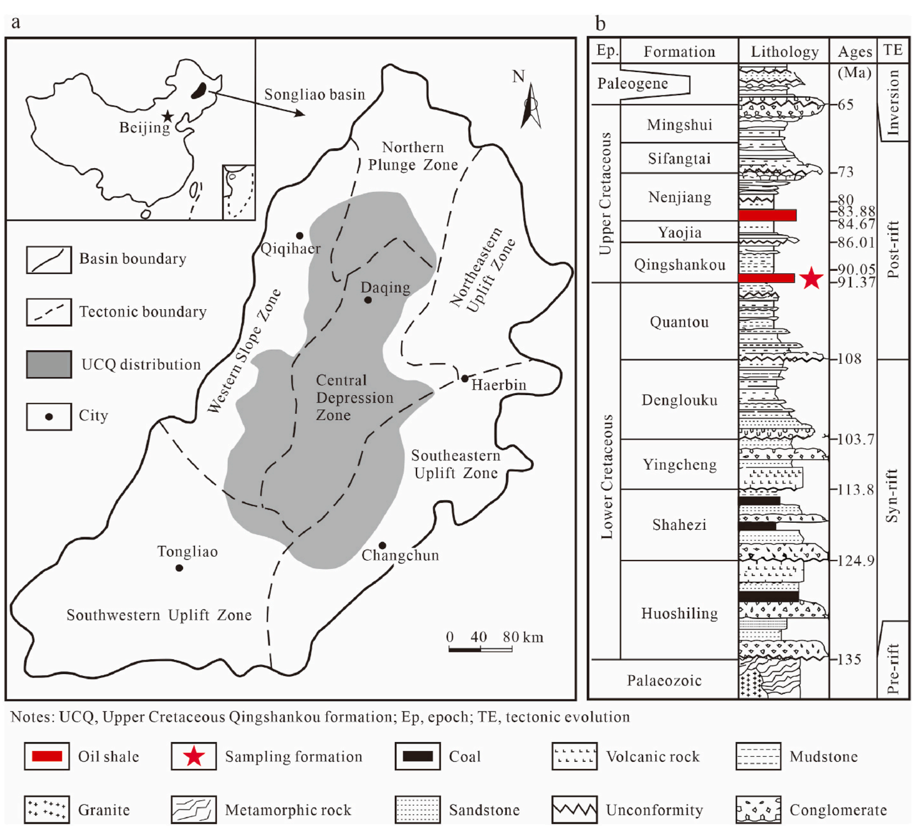

Fig. 1. Geological setting for the UCQ oil shale in the Songliao basin. a, structural units; b, stratigraphic column.

3.1. Sample collection and preparation

The samples are collected from the base of the Qingshankou formation – identified as representing ~91.37–90.05 Ma (Fig. 1b). The oil shale sample presents a total organic carbon content (TOC) of 4.8 % and represents low-maturity with a vitrinite reflectance (R_o) value of 0.95 % [27]. It mainly comprises rich clay minerals and quartz, supplemented by feldspar and trace carbonates and pyrite (Table 1). The samples were cut from the core and polished into thin sections. These samples were cut in the bedding-parallel (H2) and bedding-perpendicular directions (V1) (Fig. 2a). Accordingly, the presented pore systems from SEM observations on samples H2 and V1 are treated as the flow channels representing permeability across (H2) and along (V1) the shale bedding (Fig. 2b).

3.2. Measurements and parameter acquisition

The investigation schedule includes 1) SEM observations – to capture the pore system at elevated temperature, and 2) image processing – to transfer the SEM image captures into digital pore parameters. Pore system observations were conducted using an SEM facility embedded with a silicon heating substrate to offer a targeted elevated temperature during the measurements (Fig. 3a). SEM image capture was at six prescribed temperatures and lasting for 2h to ensure a steady state (Fig. 3b). Temperatures were incremented at 5 °C/min –to avoid thermal-shock-induced damage. Accordingly, a fixed area was selected for the continuous SEM observation for both samples (Fig. 3c), where the visual area of samples H2 and V1 are similar (~1742 μm^2). On the basis of SEM image captures, the Trainable Weka Segmentation plugin in ImageJ software was engaged to execute the machine learning operation from the SEM images (input) to yield pore morphological parameters (output), expressed as Fig. 3d and described in detail by Arganda-Carreras et al. [37] and Thilagashanthi et al. [38].

3.3. Permeability characterization

Permeability usually determine the gas/oil production capacity from geological reservoir [39,40], and various approaches may be used to calculate the permeabilities of porous media [41,42]. These include: direct measurement, such as permeability tests in closed systems [26] and indirect deduction such as from mercury intrusion porosimetry [19]. A variety of models are able to model the permeability in shale pores and are widely adopted [43]. Our approach combines the Hagen-Poiseuille model with Darcy's law to deduce the permeability of these low-maturity oil shale samples at elevated temperatures.

Using pore morphology, the Hagen-Poiseuille equation has been confirmed to be reliable in estimating the permeability of shales [44,45], indicating its applicability in this work. Accordingly, the volumetric flow rate in a single capillary (q, μm^3/s) is,

$$q = \frac{\pi d_i^4}{128\mu} \times \frac{\Delta p}{L_H} \tag{1}$$

where, Δp is the pressure difference (Pa), d_i is the capillary diameter (μm), L_H is the capillary length (μm) and μ is the oil viscosity (Pa·s).

Accordingly, the total volumetric flow rate (Q, μm^3/s) over a cross-sectional area can be regarded as the accumulation from each single capillary, q. Then,

$$Q = \sum_{i=1}^{N} q_i \tag{2}$$

where N is the total number of capillaries over the SEM cross-sectional area, and q_i is the flow capacity of a certain capillary marked as capillary i.

In addition, according to Darcy's law,

$$Q = A \times \frac{K}{\mu} \times \frac{\Delta p}{L_D} \tag{3}$$

where A is the cross-sectional area for fluid flow (μm^2), L_D is the thickness of the porous medium (μm) and and K is permeability (μm^2, i.e., ~10^3 mD).

Actually, permeability is a feature of the 3D capillary or porous medium, rather than a 2D cross-section of a pore. Therefore, this work considers a small thickness (e.g., 1 μm) for the 2D SEM captures, and under this circumstance, L_H in Eq. (1) is equal to L_D in Eq. (3) for the imaginary cube of the media (Fig. 4). In this manner, the capillary parameters in the lengthwise direction, like tortuosity, are considered to not affect the response of flow capacity. Thereafter, with the insertion of Eq. (1) and Eq. (3) into Eq. (2),

$$A \times \frac{K}{\mu} \times \frac{\Delta p}{L_H} = \frac{\pi \Delta p}{128\mu L_D} \sum_{i=1}^{N} d_i^4 \tag{4}$$

That is,

$$K = \frac{\pi}{128A} \sum_{i=1}^{N} d_i^4 \tag{5}$$

Note that the prerequisite for the establishment of Eq. (4) is that the Hagen-Poiseuille method and Darcy's approach work for the same fluid medium (same viscosity). In reality, as for shale, the cross-section of the interior pores is not circular but mostly irregular (Fig. 3c), making the direct measurement of pore diameter difficult. Thus, the concept of an equivalent hydraulic diameter (d_{ie}) of the flow channel is used to approximately characterize the diameter of the irregular shale pores [46,47], where d_{ie} is defined as,

$$d_{ie} = \frac{4S_i}{C_i} \tag{6}$$

where S_i (μm^2) and C_i (μm) are the cross-sectional area and perimeter of capillary i. As a result, by replacing the capillary diameter, d_i, with equivalent diameter, d_{ie}, Eq. (5) is,

$$K = \frac{2\pi}{A} \sum_{i=1}^{N} \left(\frac{S_i}{C_i}\right)^4 \tag{7}$$

According to Eq. (7), the cross-sectional SEM area, A, individual pore area, S_i and perimeter, C_i, of each pore may be detected by machine learning enabling the permeability, K, to be estimated, on the basis of the corresponding SEM image at each temperature.

4. Results and discussion

The permeability is first defined from the machine learning-based parameters and its relationships with the evolving pore morphology during thermal upgrading quantified. This allows the anisotropy of permeability and its variation with temperature to be defined. Furthermore, the implications of permeability evolution are analyzed with regard to restoring oil development from low-maturity oil shale subjected to in-situ heating.

Table 1
Mineral composition of the sample.

Components	Quartz	Feldspar	Carbonate mineral	Pyrite	Clay mineral	Clays		
						Illite	Chlorit	Illite/smectite mixed
Content (%)	36.4	16.6	7.9	5.2	33.9	54	27	19

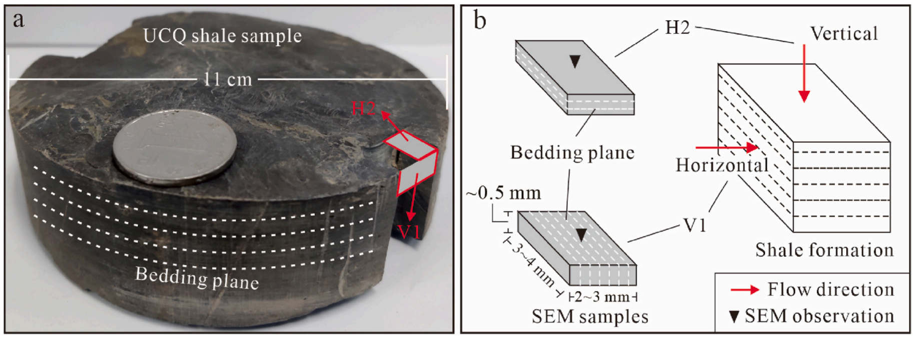

Fig. 2. Sample preparation. a, collected shale core – same to that in Liu et al. [27]; b, prepared SEM samples relative to bedding-perpendicular (H2) and -parallel (V1) flow directions.

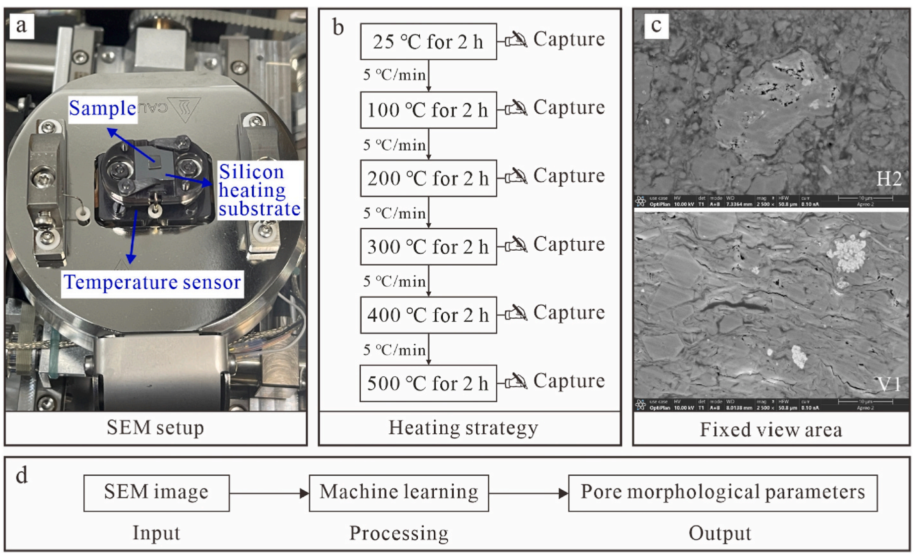

Fig. 3. SEM observations with heating schedule to observe changes in pore morphology. a, SEM heating substrate; b, heating schedule and SEM captures; c, SEM fixed view area of two samples. d, processing methods from SEM images to digital parameters. Details exhibited in Liu et al. [27].

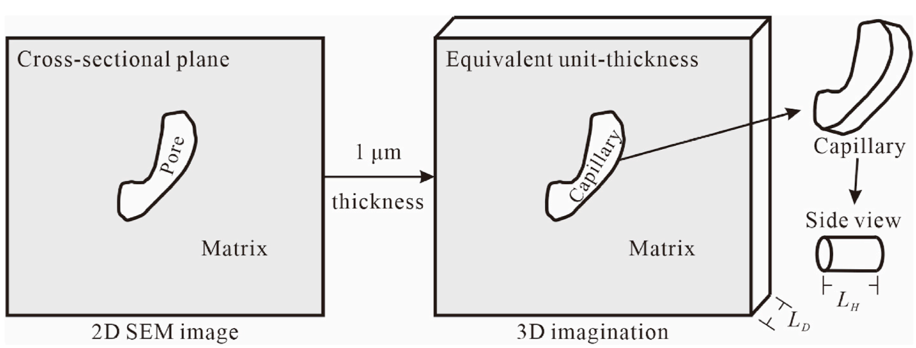

Fig. 4. The transition from a 2D plane to a 3D expression.

4.1. Permeability evolution with temperature

Using measurements from Liu et al. [27], Eq. (7) enables the permeability, K, to be determined, as exhibited in Fig. 5, to present the growth in permeability with increasing temperature. Seepage channels are enhanced by the thermal upgrading. In comparison, the growth in permeability for sample V1 is continuous and increases by ~2 times, while that for sample H2 fluctuates and increases by ~1.5 times (Fig. 5). The K enhancement results from the newly-formed pore space resulting from the combined effects of pyrolysis of organic matter, the enlarged pore space by dehydration-induced matrix shrinkage of the clay minerals and other improvements in pore space connectivity such as in connecting original disconnected or plugged pores at elevated temperature. The occasional decrease in K over some temperature intervals (e.g. 100–200 °C and 300–400 °C for sample H2) is a frequent phenomenon, also measured by He et al. [25]. In this case, it is speculated that the matrix swelling stimulated by the thermal expansion effect directs the K variation at high temperature, compressing some channels. However, the K values are the result of multi-factor couplings – with the dominant processes controlling the result.

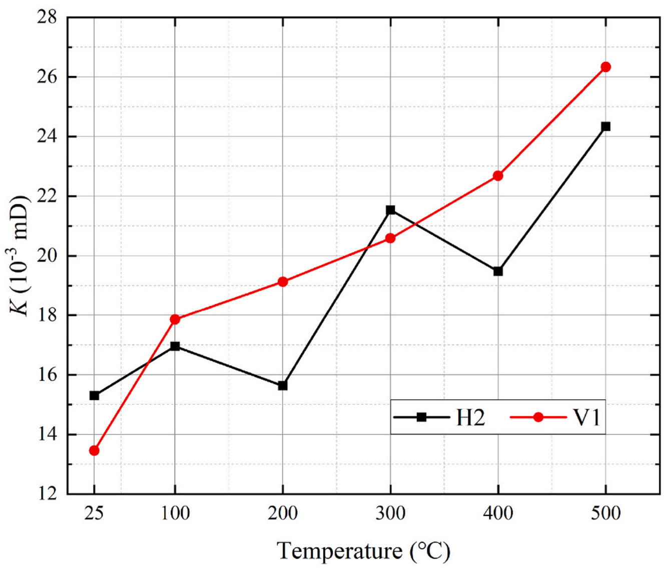

Fig. 5. Calculated permeability for two samples and its variation with temperature according to Eq. (7).

4.2. Pore quantity and area influencing permeability

Previous SEM images and resulting machine learning outputs increment pore quantity (N) for both samples H2 and V1 at elevated temperature from 25 to 500 °C [27]. Intuitively, more pores offer more possible channels for seepage behavior and thus support K enhancement, which is revealed by the N-K correlation (Fig. 6). Relatively, the correlation coefficient (R^2 value) suggests that the N-K relationship for sample V1 is a bit stronger than that for sample H2 (Fig. 6), which is possibly due to more heating-induced pores contributing to the permeability calculated for sample V1 relative to sample H2. This phenomenon suggests that more newly developed pores participate in the seepage behavior in the direction parallel to shale bedding (revealed by sample V1), compared to the direction perpendicular to shale bedding (revealed by sample H2), when the shale experiences thermal upgrading; regarding this issue, however, more efforts are required to clarify the in-depth mechanism.

As for the pore area, it corresponds to the cross-sectional area of a single capillary, exhibited by the conceptual scheme of Fig. 4. For a certain capillary, a greater area indicates a wider section to accommodate seepage; therefore, there is a basic positive correlation between the total pore area and the K values, for both samples H2 and V1 (Fig. 7). This indicates that elevated temperature ensures a greater total pore area over the SEM cross-section, which results in this positive feedback for the seepage capacity (K values). Besides, similar with the N-K correlation coefficient (Fig. 6), the R^2 value of the relationship between total pore area and K for sample V1 is greater, compared to that for sample H2 (Fig. 7). This phenomenon further suggests that more newly developed pores increase seepage capacity in the bedding-parallel direction than bedding-perpendicular during the in-situ heating– a speculation that requires confirmation.

4.3. Pore fractal dimension affecting permeability

Finally, fractal theory is introduced to enable the fractal dimension (D_f) to be determined and the coupling relationship between D_f values and permeabilities to be determined at each elevated temperature.

4.3.1. Fractal dimension

The fractal dimension, D_f, contributes to understanding the complexity of the pore system [48,49], and can be determined by many methods, including: low-temperature N_2 adsorption [50], low-field NMR [51], mercury intrusion porosimetry [52], and 3D X-ray CT reconstruction [53]. The parameters of pore area, S (μm^2), pore perimeter, C (μm), and pore morphology measured from SEM captures are also capable of inferring the D_f values as [54,55],

$$\log C = \frac{D_f}{2} \log S + c_1 \tag{8}$$

where log C presents a linear correlation with log S with a slope of $D_f/2$ and an intercept of c_1, by which D_f is recovered. $D_f = 1$ indicates a perfect uniformity (like a line) regarding the pore structure, while a greater D_f (up to 2) suggests a more complex pore microstructure, and D = 2 represents a filled plane (i.e. a surface).

On the basis of the S and C values recovered from the machine learning outputs [27], Eq. (8) yields the $\log C - \log S$ correlations of samples H2 and V1 at each temperature, where linear relationships hold (i.e. all R^2 values are greater than 0.96 (Fig. 8)). Accordingly, the D_f values are recovered and listed in Fig. 9, in which a slight increase in D_f occurs with increasing temperature for the two samples (H2 and V1). The D_f value increase from 1.25 to 1.35 for sample H2 and from 1.37 to

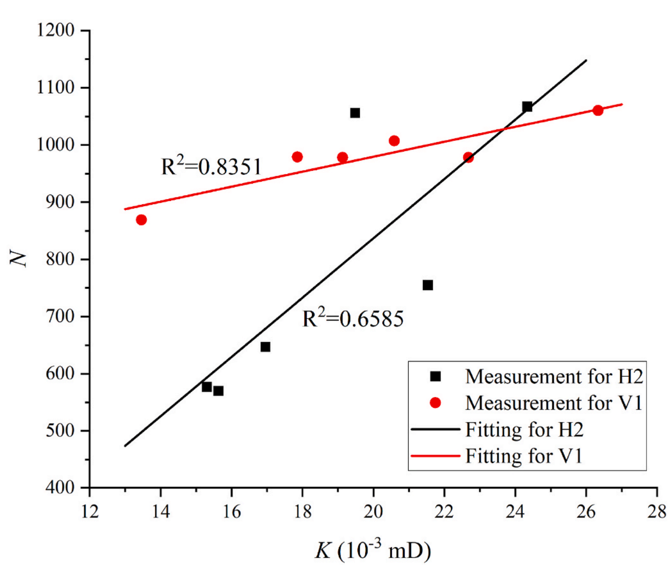

Fig. 6. Correlation between pore quantity (N) and permeability (K).

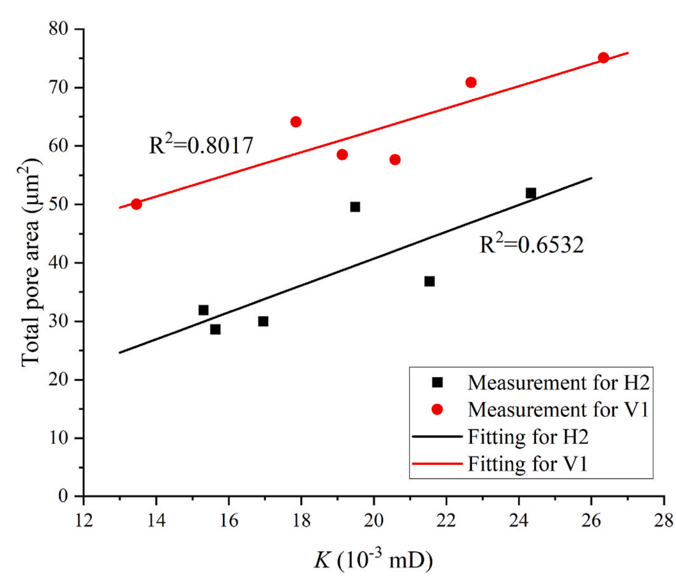

Fig. 7. Correlation between total pore area and permeability (K).

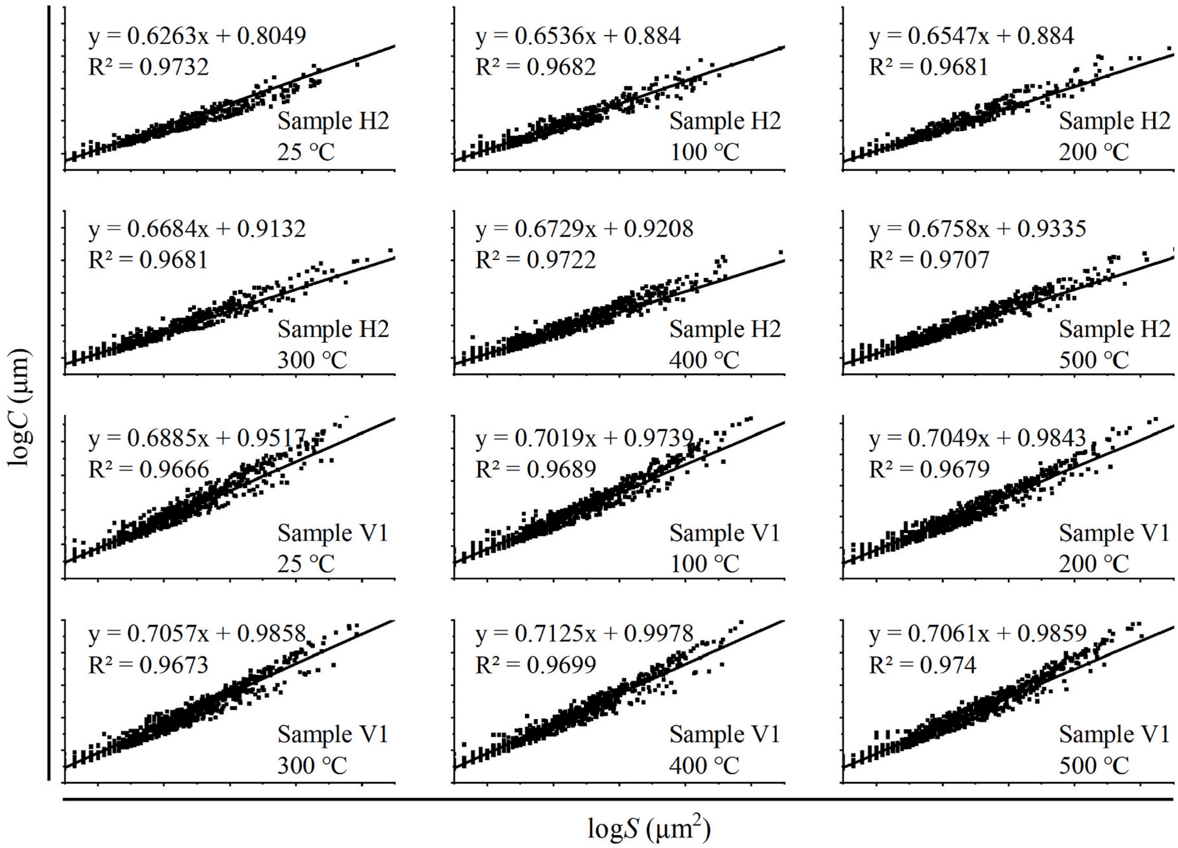

Fig. 8. Linear correlation between log C and log S for to determine fractal dimension (D_f) at different temperatures.

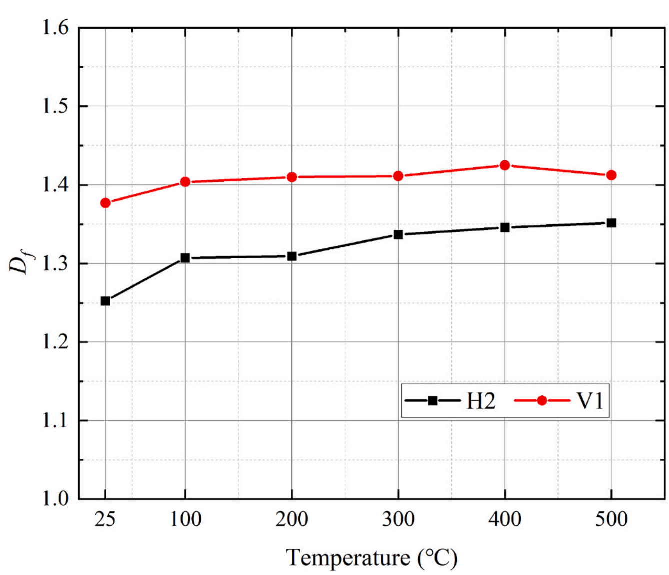

Fig. 9. Fractal dimension (D_f) of two samples recovered from Eq. (8) and its variation with temperature.

1.41 for sample V1, suggesting that the heating-induced pores complicate the pore microstructure in a complex manner. In contrast, the D_f values for sample V1 are slightly larger than those for sample H2 at each temperature, indicating a more complex microstructure of pores in the cross-section of bedding-perpendicular direction than the bedding-parallel direction.

4.3.2. Relationship between fractal dimension and permeability

With respect to the relationship between fractal dimension and permeability, previous observations tend to consider that a greater D_f represents a more complex pore system, limiting flow and representing a reduced permeability [56]. However, some observations to the contrary define an overall positive relationship between fractal dimension and permeability [57] – leaving linkages ambiguous. In this work, the D_f values correlate approximately positively with K, although the R^2 is only ~0.65 (Fig. 10). Heating ensures an increase in the number of pores (N) and the total pore area, inferring an enhancement in seepage (increased

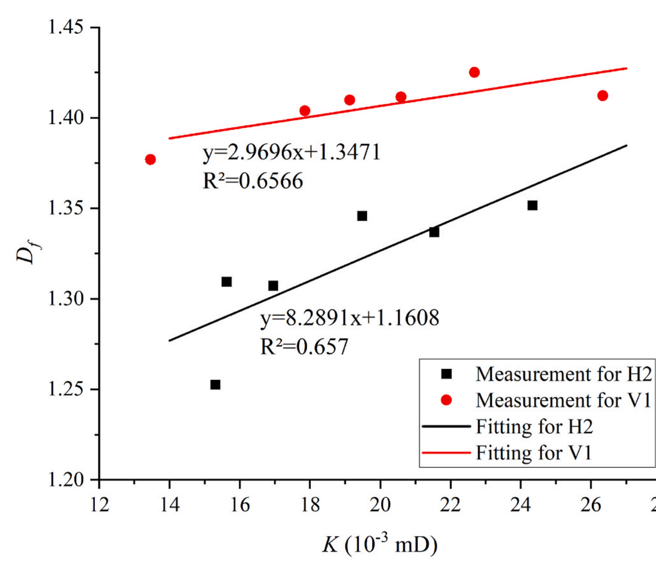

Fig. 10. Correlation between fractal dimension (D_f) and permeability (K).

K) (Figs. 6 and 7); meanwhile, there is also a slight increase in D_f that corresponds to a more complex pore system (Fig. 9) – seemingly detrimental to seepage. Therefore, the multiple pore parameters affected by the elevated temperature together determine the seepage behavior (i.e, K value), resulting in that presented fractal dimension exhibiting a generally positive relationship with permeability.

4.4. Description on anisotropy degree of permeability

Anisotropic permeability is an inherent attribute for shales and significantly influences seepage behavior [58]. The K values derived from sample V1 are greater than those from sample H2 (Fig. 11a), and conforms to conventional understanding that the bedding-parallel permeability is greater than that bedding-perpendicular – as exhibited in Fig. 2b. However, the preponderance of horizontal permeability is inconsistent (compared to vertical permeability) for observations as 25 and 300 °C (Fig. 11b). Shale bedding significantly affects seepage [15] and an coefficient of anisotropic permeability (R_{AK}) may be used to define the degree of anisotropy of permeability. R_{AK} is described as,

$$R_{AK} = \frac{K_{V1}}{K_{H2}} \tag{9}$$

where K_{V1} and K_{H2} represent the permeabilities calculated from samples V1 and H2, and corresponding to bedding-parallel and bedding-perpendicular permeabilities, respectively.

The R_{AK} values (less than 2) indicate minor anisotropy of K_{V1} and K_{H2}, much smaller than those in Wang et al. [15] where the R_{AK} was ~100~400. Nevertheless, the outcomes in this work are from a micro-section in SEM view, and the two observed areas are artificially selected, indicating that other areas could be more anisotropic.

Furthermore, this work puts forward a new concept, that is, an aggregation degree of permeability (A_K), to evaluate the degree of participation of all pores in contributing to the seepage behavior. Herein, the A_K is described as the proportion of pores that contribute to half of the permeability K relative to the entire pore distribution as,

$$A_K = \frac{\text{Quantity of pores for } 50\%K}{\text{Whole pore quantity}} \times 100\% \tag{10}$$

where a greater A_K (up to 50 %) represents a higher participation of detected pores in the seepage behavior and thus suggest that more pores contribute to the K value, while a smaller one indicates that fewer pores dominate the K value.

For these samples (Fig. 12), the A_K values are generally small and are all lower than 8 %, suggesting that the seepage capacity (K value) is dominated by the minority of all pores for all temperatures. The A_K value of sample V1 is slightly greater than that of sample H2, noting a higher proportion of pores in the section in the bedding-perpendicular direction, rather than in the bedding-parallel direction, contributes to K. Fig. 12 also shows that the A_K value trends upward for sample V1, while that holds a gross downward tendency for sample H2 at elevated temperature. This phenomenon signals that in-situ thermal upgrading tends to amplify the anisotropic A_K performance. That is to say, at elevated temperature, a greater proportion of pores contributes to the K value of sample V1, while the opposite trend applies to sample H2. This is because heating creates smaller new pores (compared to the original pores) that little influence the K for sample H2 while larger pores contribute to the K for sample V1 – as illustrated by Liu et al. [27].

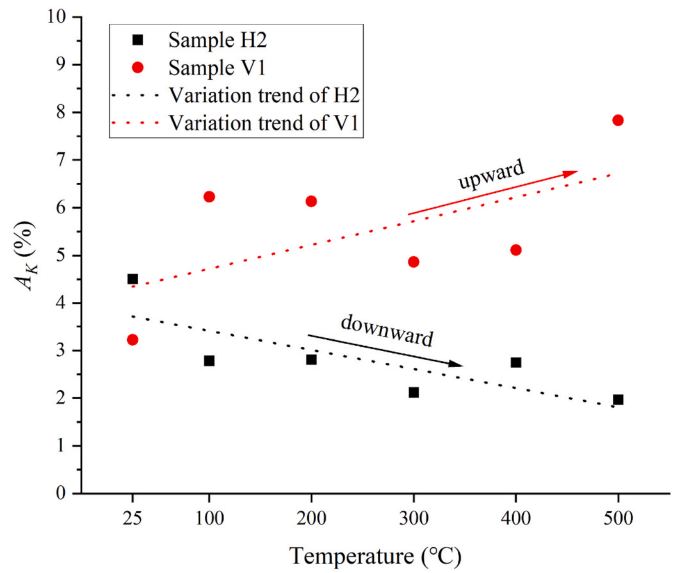

Fig. 12. Aggregation degree of permeability (A_K) for the two samples.

4.5. Implications for oil recovery

Five modes of pore space evolution were observed during the thermal upgrading [27]. Accordingly, mechanisms influencing permeability are preliminarily investigated. Heating-induced pore compression degrades permeability, while other heating-induced pore evolution behaviors improve permeability. These include the formation of new pores, the interconnection of pores which were previously disconnected or plugged, extended pore space and enlarged pore space (Fig. 13). Since the purpose of in-situ heating is to recover oil from low-maturity oil shales, it is important to correctly and effectively deploy heating wells relative to the production wells. Taking the mode of a single heating injection well surrounded by four oil production wells as an example (Fig. 14), the direction horizontal to the shale bedding is of higher permeability and thus the permeability isolines are a series of concentric ellipses – the closer to the heating well, the higher the permeability. As the permeability usually controls the enhancement in oil production, the production should follow the tendency of the permeability evolution. Moreover, since a higher temperature indicates a further elevated

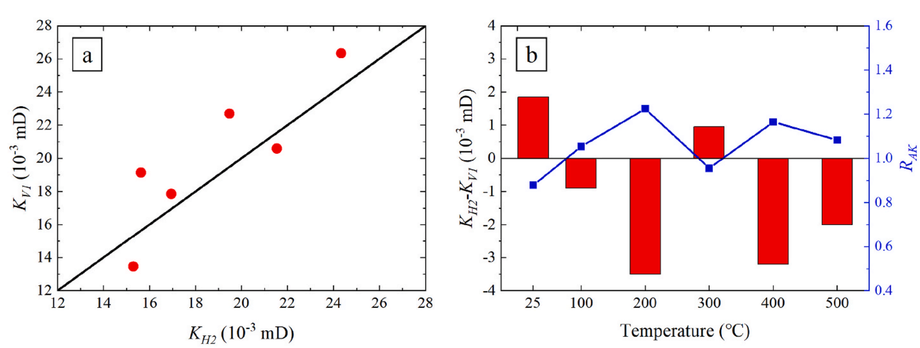

Fig. 11. Anisotropic permeability. a, comparison between permeabilities of samples H2 (K_{H2}) and V1 (K_{V1}); b, anisotropic coefficient of permeability (R_{AK}).

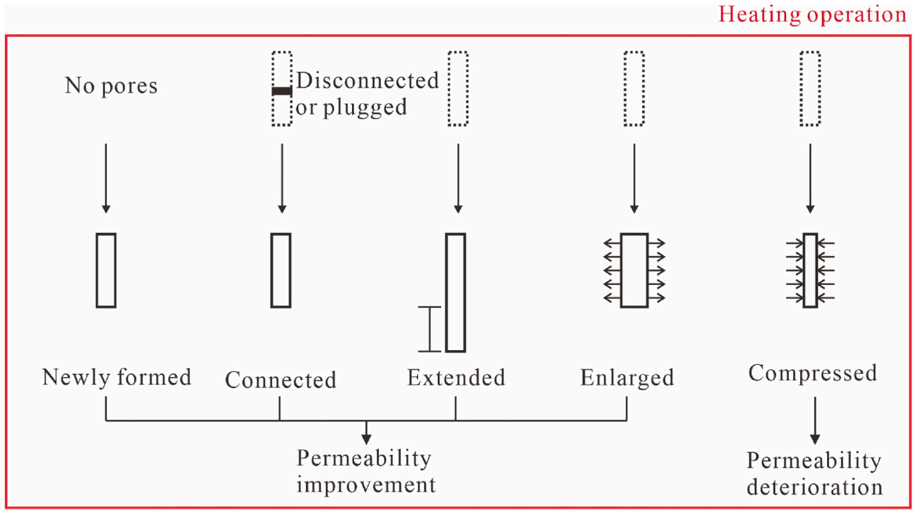

Fig. 13. Schematic of the influence of heating on permeability evolution. Modified from Liu et al. [27].

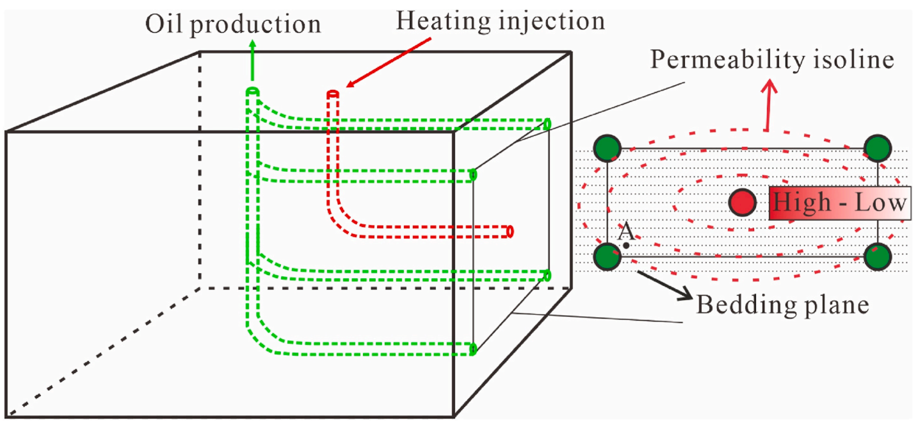

Fig. 14. Schematic for the relative location of heating injection well and oil production wells.

permeability, the temperature in the area close to production well (e.g., point A in Fig. 14) determines the lower threshold of permeability and thus controls the seepage capacity of the entire heating, hence drainage area. Therefore, permeability evolution modeling at elevated temperature is the prerequisite for the effective well deployment and the efficient restoring oil development.

5. Conclusions

In-situ thermal upgrading significantly increases the permeability, K, of low-maturity oil shale, for both the bedding-parallel and bedding-perpendicular directions. The K increase largely results from the heating-induced augmentation of pore quantity, N, and total pore area (over an SEM cross-section), which significantly increases permeability due to the scaling of permeability with equivalent pore diameter squared. In comparison, the bedding-perpendicular sample (V1) presents a stronger correlation between K and N value (or total pore area) than the bedding-parallel sample (H2).

Revealed by the fractal dimension, D_f, pores from the bedding-perpendicular sample (V1) exhibits a more complex microstructure than bedding-parallel sample (H2) under all temperature conditions; meanwhile, the elevated temperatures only slightly augment pore microstructures. An weak positive correlation ($R^2 = \sim 0.65$) of D_f-K exists for both samples, likely due to the heating-induced D_f increase is accompanied by an increase in the number of pores (N) and total pore area – thus, multiple factors co-determine the K value evolution.

Permeability is persistently anisotropic during the entire heating process, where the K value parallel to bedding is always larger. However, the degree of anisotropy varies at elevated temperature, supported by the anisotropic coefficient of permeability, R_{AK}. The resulting permeability is mainly contributed by the minority pores – 50 % of the permeability K originates from <8 % pores in the SEM section. At elevated temperature, an increased number of pores in the bedding-parallel direction participate in the seepage behavior, with the converse true for bedding-perpendicular.

During the thermal upgrading of low-maturity oil shales, five modes of pore space evolution jointly affect the permeability, K, where heating-induced pore compression reduces the permeability. Since a higher temperature is shown to generally indicate an enhanced permeability, the actual temperature transmitted to the region close to the production well determines the lower threshold of permeability and thus controls the hydrocarbon recovery capacity of the ensemble heating system. Such a permeability-based simulation significantly informs the deployment of heating systems for oil production and for the effective recovery of tight oil.

CRediT authorship contribution statement

Bo He: Writing – original draft, Methodology, Data curation. **Lingzhi Xie:** Supervision, Methodology, Conceptualization. **Xin Liu:** Validation, Resources. **Jun Liu:** Writing – review & editing, Writing – original draft, Supervision, Funding acquisition, Conceptualization. **Derek Elsworth:**

Writing – review & editing, Methodology.

Declaration of competing interest

The authors declare that the research was conducted in the absence of any commercial or financial relationships that could be construed as a potential conflict of interest.

Acknowledgements

This study was financially supported by the National Key Research and Development Program of China (Grant No. 2022YFE0129800), the National Natural Science Foundation of China (Grant No. 42202204), and the Natural Science Foundation of Chongqing, China (Grant No. CSTB2023NSCQ-LZX0036). The authors gratefully acknowledge Dr. Xi Wu from the Analytical & Testing Center of Sichuan University for his help with the component characterization.

References

[1] R. Aguilera, Flow Units: from conventional to tight-gas to shale-gas to tight-oil to shale-oil reservoirs, SPE Reservoir Eval. Eng. 17 (2) (2014) 190–208.
[2] L.H. Hou, X. Luo, Z.Y. Zhao, L.J. Zhang, Identification of oil produced from shale and tight reservoirs in the permian lucaogou shale sequence, jimsar sag, junggar basin, NW China, ACS Omega 6 (3) (2021) 2127–2142.
[3] L. Li, S. Ma, X. Liu, J. Liu, Y. Lu, P. Zhao, et al., Coal measure gas resources matter in China: review, challenges, and perspective, Phys. Fluids 36 (7) (2024) 071301.
[4] D. Liu, Y. Yao, Y. Chang, Measurement of adsorption phase densities with respect to different pressure: potential application for determination of free and adsorbed methane in coalbed methane reservoir, Chem Eng J 446 (2022) 137103.
[5] M.H. Vatter, S.A. Van Vactor, T.C. Coburn, Price responsiveness of shale oil: a bakken case study, Nat Resour Res 31 (2022) 713–734.
[6] W. Zhao, M. Guan, W. Liu, C. Bian, Y. Li, X. Wang, et al., Low-to-medium maturity lacustrine shale oil resource and in-situ conversion process technology: recent advances and challenges, Advances in Geo-Energy Research 12 (2) (2024) 81–88.
[7] Y. Xu, Z.M. Lun, Z.J. Pan, H.T. Wang, X. Zhou, C.P. Zhao, et al., Occurrence space and state of shale oil: a review, J. Petrol. Sci. Eng. 211 (2022) 110183.
[8] S. Zhao, X. Zhao, Q. Jiang, C. Yuan, H. Wang, L. Yang, et al., Thermo-oxidative characteristics, kinetic triplets, and auto-ignition potential of shale oil during air injection, Geoenergy Science and Engineering 239 (2024) 212984.
[9] X.N. Wang, J.R. Li, W.Q. Jiang, H. Zhang, Y.L. Feng, Z. Yang, Characteristics, current exploration practices, and prospects of continental shale oil in China, Advances in Geo-Energy Research 6 (6) (2022) 454–459.
[10] J. Zhao, L. Wang, S.M. Liu, Z.Q. Kang, D. Yang, Y.S. Zhao, Numerical simulation and thermo-hydro-mechanical coupling model of in situ mining of low-mature organic-rich shale by convection heating, Advances in Geo-Energy Research 6 (6) (2022) 502–514.
[11] Z. Lei, Y. Zhang, Z. Yang, Y. Shi, H. Zhang, X. Li, et al., Numerical simulation of oil shale in-situ exploration productivity comparison between steam injection and electrical heating, Appl. Therm. Eng. 238 (2024) 121928.
[12] X. Bai, J. Li, X. Liu, R. Wang, S. Ma, F. Yang, et al., Evolution of the anisotropic thermophysical performance for low-maturity oil shales at an elevated temperature and its implications for restoring oil development, Energ Fuel 38 (16) (2024) 15216–15224.
[13] Z.Q. Kang, D. Yang, Y.S. Zhao, Y.Q. Hu, Thermal cracking and corresponding permeability of fushun oil shale, Oil Shale 28 (2) (2011) 273–283.
[14] J. Liu, Y.B. Yao, D. Elsworth, Morphological complexity and azimuthal disorder of evolving pore space in low-maturity oil shale during in-situ thermal upgrading and impacts on permeability, Pet Sci 21 (5) (2024) 3350–3362.
[15] G.Y. Wang, D. Yang, Y.S. Zhao, Z.Q. Kang, J. Zhao, X.D. Huang, Experimental investigation on anisotropic permeability and its relationship with anisotropic thermal cracking of oil shale under high temperature and triaxial stress, Appl. Therm. Eng. 146 (2019) 718–725.
[16] B. Chen, J.T. Cai, X.R. Chen, D. Wu, Y. Pan, A review on oil shale in-situ mining technologies: opportunities and challenges, Oil Shale 41 (1) (2024) 1–25.
[17] Z. Wang, W. Fan, H. Sun, J. Yao, G. Zhu, L. Zhang, et al., Multiscale flow simulation of shale oil considering hydro-thermal process, Appl. Therm. Eng. 177 (2020) 115428.
[18] D.M. Niu, P.C. Sun, L. Ma, K.A. Zhao, C. Ding, Porosity evolution of Minhe oil shale under an open rapid heating system and the carbon storage potentials, Renew. Energy 205 (2023) 783–799.
[19] Z. Cui, M.D. Sun, E. Mohammadian, Q.H. Hu, B. Liu, M. Ostadhassan, et al., Characterizing microstructural evolutions in low-mature lacustrine shale: a comparative experimental study of conventional heat, microwave, and water-saturated microwave stimulations, Energy 295 (2024) 130797.
[20] J. Zhang, Y. Tang, D. He, P. Sun, X. Zou, Full-scale nanopore system and fractal characteristics of clay-rich lacustrine shale combining FE-SEM, nano-CT, gas adsorption and mercury intrusion porosimetry, Appl. Clay Sci. 196 (2020) 105758.
[21] S.T. Xu, Y.H. Sun, Q.C. Yang, H. Wang, S.J. Kang, W. Guo, et al., Product migration and regional reaction characteristics in the autothermic pyrolysis in-situ conversion process of low-permeability Huadian oil shale core, Energy 283 (2023) 128525.
[22] S. Tian, J. Zhou, X. Xian, Q. Gan, C. Zhang, Z. Dong, et al., The impact of supercritical CO_2 exposure time on the effective stress law for permeability in shale, Energy 284 (2023) 129334.
[23] M. Li, M. Wang, L. Zhang, Q. Wang, X. Wang, X. Li, et al., Understanding pore space and oil content of liquid-rich shale in the southern Bohai Sea, China, Geoenergy Science and Engineering 233 (2024) 212552.
[24] L. Wang, D. Yang, Z.Q. Kang, Evolution of permeability and mesostructure of oil shale exposed to high-temperature water vapor, Fuel 290 (2021) 119786.
[25] W.Y. He, Q.A. Meng, T.F. Lin, R. Wang, X. Liu, S.M. Ma, et al., Evolution features of in-situ permeability of low-maturity shale with the increasing temperature, Cretaceous Nenjiang Formation, northern Songliao Basin, NE China, Pet Explor Dev 49 (3) (2022) 516–529.
[26] L. Wang, J.Z. Su, D. Yang, Study on pyrolysis-mechanics-seepage behavior of oil shale in a closed system subject to real-time temperature variations, Materials 15 (2022) 5368.
[27] J. Liu, X. Bai, D. Elsworth, Evolution of pore systems in low-maturity oil shales during thermal upgrading - quantified by dynamic SEM and machine learning, Pet Sci 21 (2024) 1739–1750.
[28] X.N. Tong, J.F. Hu, D.P. Xi, M.B. Zhu, J.Z. Song, P.A. Peng, Depositional environment of the Late Santonian lacustrine source rocks in the Songliao Basin (NE China): implications from organic geochemical analyses, Org. Geochem. 124 (2018) 215–227.
[29] J.L. Jia, A. Bechtel, Z.J. Liu, S.A.I. Strobl, P.C. Sun, R.F. Sachsenhofer, Oil shale formation in the upper cretaceous nenjiang formation of the Songliao basin (NE China): implications from organic and inorganic geochemical analyses, Int. J. Coal Geol. 113 (2013) 11–26.
[30] M. Wang, S.F. Lu, H.T. Xue, Kinetic simulation of hydrocarbon generation from lacustrine type I kerogen from the Songliao Basin: model comparison and geological application, Mar Pet Geol 28 (9) (2011) 1714–1726.
[31] Z.Q. Feng, C.Z. Jia, X.N. Xie, S. Zhang, Z.H. Feng, T.A. Cross, Tectonostratigraphic units and stratigraphic sequences of the nonmarine Songliao basin, northeast China, Basin Res. 22 (1) (2010) 79–95.
[32] C.S. Wang, Z.G. Feng, L.M. Zhang, Y.J. Huang, K. Cao, P.J. Wang, et al., Cretaceous paleogeography and paleoclimate and the setting of SKI borehole sites in Songliao Basin, northeast China, Palaeogeogr Palaeocl 385 (2013) 17–30.
[33] R.Q. Chen, F. Shang, Y.S. Cao, L. Song, Z. Li, A comparative study of oil shale deposition in the Upper Cretaceous Nenjiang Formation, NE China: evidence from petrographic and geochemical analyses, J. Petrol. Sci. Eng. 219 (2022) 111130.
[34] J.J. Xu, Z.J. Liu, A. Bechtel, Q.T. Meng, P.C. Sun, J.L. Jia, et al., Basin evolution and oil shale deposition during Upper Cretaceous in the Songliao Basin (NE China): implications from sequence stratigraphy and geochemistry, Int. J. Coal Geol. 149 (2015) 9–23.
[35] S. Zhang, B. Zhang, X. Wang, Z. Feng, K. He, H. Wang, et al., Gulong shale oil enrichment mechanism and orderly distribution of conventional– unconventional oils in the Cretaceous Qingshankou Formation, Songliao Basin, NE China, Pet Explor Dev 50 (2023) 1045–1059.
[36] D.J. Hou, M.W. Li, Q.H. Huang, Marine transgressional events in the gigantic freshwater lake Songliao: paleontological and geochemical evidence, Org. Geochem. 31 (7–8) (2000) 763–768.
[37] I. Arganda-Carreras, V. Kaynig, C. Rueden, K.W. Eliceiri, J. Schindelin, A. Cardona, et al., Trainable Weka Segmentation: a machine learning tool for microscopy pixel classification, Bioimage Informatics 33 (2017) 2424–2426.
[38] T. Thilagashanthi, K. Gunasekaran, K.S. Satyanarayanan, J.J. Klemes, Microstructural pore analysis using SEM and ImageJ on the absorption of treated coconut shell aggregate, J Cleaner Prod 324 (2021) 129217.
[39] K. Yu, K. Zhao, Y. Ju, A comparative study of the permeability enhancement in coal and clay-rich shale by hydraulic fracturing using nano-CT and SEM image analysis, Appl. Clay Sci. 218 (2022) 106430.
[40] G. Wang, D. Yang, Y. Zhao, Z. Kang, J. Zhao, X. Huang, Experimental investigation on anisotropic permeability and its relationship with anisotropic thermal cracking of oil shale under high temperature and triaxial stress, Appl. Therm. Eng. 146 (2019) 718–725.
[41] L.H. Zhang, B.C. Shan, Y.L. Zhao, Z.L. Guo, Review of micro seepage mechanisms in shale gas reservoirs, Int J Heat Mass Transfer 139 (2019) 144–179.
[42] S. Akilu, E. Padmanabhan, Z. Sun, A review of transport mechanisms and models for unconventional tight shale gas reservoir systems, Int J Heat Mass Transfer 175 (2021) 121125.
[43] R.H. Cui, S.M. Hassanizadeh, S.Y. Sun, Pore-network modeling of flow in shale nanopores: network structure, flow principles, and computational algorithms, Earth Sci. Rev. 234 (2022) 104203.
[44] H. Wang, Y.L. Su, W.D. Wang, L. Li, G.L. Sheng, S.Y. Zhan, Relative permeability model of oil-water flow in nanoporous media considering multi-mechanisms, J. Petrol. Sci. Eng. 183 (2019) 106361.
[45] L. Zhao, G.C. Wu, J.H. He, Fractal approach to flow through porous material, Int J Nonlin Sci Num 10 (7) (2009) 897–901.
[46] H.Q. Lian, W. Ran, X.X. Xia, Research on SEM image processing and micro-information extraction technology, Coal Technol. 34 (10) (2015) 119–122.
[47] T. Jiang, W. Xu, Z.Z. Su, Alculation and analysis of permeability of sandstone SEM image by small island method, Journal of North China Institute of Science and Technology 15 (5) (2018) 54–59.
[48] X. Yang, Y.P. Du, Q. Xu, F.T. Wu, T. Zhou, C.Y. Zhao, Pores integrated fractal (PIF) analysis on transportation in porous media considering spatial distribution of pores and genuine tortuosity, Int J Heat Mass Transfer 187 (2022) 122528.

[49] D.Y. Ye, G.N. Liu, F.T. Wang, F. Gao, T.T. Yang, J.Y. Zhu, Fractal hydrological-thermal-mechanical analysis of unconventional reservoir: a fracture-matrix structure model for gas extraction, Int J Heat Mass Transfer 202 (2023) 123670.
[50] J. Liu, Y. Yao, D. Liu, Y. Cai, J. Cai, Comparison of pore fractal characteristics between marine and continental shales, Fractals 26 (2) (2018) 1840016.
[51] S.J. Zheng, Y.B. Yao, D.M. Liu, Y.D. Cai, Y. Liu, Characterizations of full-scale pore size distribution, porosity and permeability of coals: a novel methodology by nuclear magnetic resonance and fractal analysis theory, Int. J. Coal Geol. 196 (2018) 148–158.
[52] P.H. Su, Z.H. Xia, L.C. Qu, W. Yu, P. Wang, D.W. Li, et al., Fractal characteristics of low-permeability gas sandstones based on a new model for mercury intrusion porosimetry, J. Nat. Gas Sci. Eng. 60 (2018) 246–255.
[53] H.J. Wang, S.B. Chen, S.J. Zhang, C.X. Zhang, Y. Wang, G.F. Yi, et al., Study on fracture characteristics in coal and shale for coal-measure gas reservoir based on 3D CT reconstruction and fractal features, Front. Earth Sci. 17 (2) (2023) 514–526.
[54] C. Liu, B. Shi, J. Zhou, C.S. Tang, Quantification and characterization of microporosity by image processing, geometric measurement and statistical methods: application on SEM images of clay materials, Appl. Clay Sci. 54 (1) (2011) 97–106.
[55] J.F. Qi, W.H. Sui, C.L. Zhang, J.S. Xu, Calculation and analysis of the porosity and fractal dimension of red stratum sandstone based on SEM images processing, J. Eng. Geol. 22 (2014) 339–345 (In Chinese with English abstract).
[56] Y.D. Hong, B.Q. Lin, C.J. Zhu, H. Li, Influence of microwave energy on fractal dimension of coal cores: implications from nuclear magnetic resonance, Energ Fuel 30 (12) (2016) 10253–10259.
[57] Y.X. Xia, J.C. Cai, E. Perfect, W. Wei, Q. Zhang, Q.B. Meng, Fractal dimension, lacunarity and succolarity analyses on CT images of reservoir rocks for permeability prediction, J Hydrol 579 (2019) 124198.
[58] J. Liu, L.Z. Xie, B. He, Q. Gan, P. Zhao, Influence of anisotropic and heterogeneous permeability coupled with in-situ stress on CO_2 sequestration with simultaneous enhanced gas recovery in shale: quantitative modeling and case study, Int J Greenhouse Gas Control 104 (2021) 103208.